Ca_2CuWO_6: Triclinically-distorted double perovskite with low-dimensional magnetic behavior

Xuan Liang [a,b], Kazunari Yamaura [a,b], Alexander A. Tsirlin [c], Alexei A. Belik [a,*]

[a] *Research Center for Materials Nanoarchitectonics (MANA), National Institute for Materials Science (NIMS), Namiki 1-1, Tsukuba, Ibaraki 305-0044, Japan*

[b] *Graduate School of Chemical Sciences and Engineering, Hokkaido University, North 10 West 8, Kita-ku, Sapporo, Hokkaido 060-0810, Japan*

[c] *Felix Bloch Institute for Solid-State Physics, Leipzig University, 04103 Leipzig, Germany*

* Corresponding author.

E-mail address: Alexei.Belik@nims.go.jp (A.A. Belik)

Abstract

$A_2CuB'O_6$ double perovskites with A = Sr and Ba and B′ = W, Te, and Mo have received a lot of attention in the literature as material candidates for the spin-liquid ground state and frustrated spin lattices. However, Ca analogues have not been reported yet. In this work, the Ca_2CuWO_6 double perovskite was synthesized by a high-pressure, high-temperature method at 6 GPa and between 1370 and 2020 K. The crystal structure was studied by synchrotron powder X-ray diffraction between 100 K and 1000 K. Ca_2CuWO_6 crystallizes in the triclinic space group $P\bar{1}$ between 100 K and 1000 K with the onset of partial decomposition above 750 K. Room-temperature lattice parameters are a = 5.68435 Å, b = 7.51261 Å, c = 5.49548 Å, α = 90.0703°, β = 94.7634°, and γ = 90.2311°. Ca_2CuWO_6 demonstrates low-dimensional magnetic properties with the broad maximum of the magnetic susceptibility around 60 K caused by the dominant second-neighbor interactions within the deformed square planes of the Cu^{2+} ions. A long-range antiferromagnetic order takes place at T_N = 32 K. A magnetic field-induced transition was observed at 28 kOe (at 2 K and 5 K), 29 kOe (at 10 K), 30 kOe (at 15 K), 32 kOe (at 20 K), and 36 kOe (at 25 K). Solid solutions $Ca_{2-x}Sr_xCuWO_6$ with x = 0.5, 1, and 1.5 were also prepared. The x = 0.5 and 1 samples crystallize in the space group $P\bar{1}$ at room temperature, while the x = 1.5 sample has monoclinic symmetry (space group $P2_1/n$). They also show low-dimensional magnetic behavior, T_N = 32–34 K, and magnetic field-induced transitions.

Keywords: double perovskites; low-dimensional magnets; antisite disorder; crystal structures; high-pressure synthesis

1. Introduction

B-site-ordered double perovskites with the stoichiometric formula of $A_2BB'O_6$ have attracted extensive attention [1] owing to their novel magnetic and electrical properties, such as colossal magnetoresistance [2], superconductivity [3], and half-metallic behaviors [4]. Among them, double perovskites with A = Ca^{2+}, Sr^{2+}, and Ba^{2+}, B = divalent 3*d* magnetic or nonmagnetic transition metal cations (*M*), and B′ = W^{6+} (A_2MWO_6) have been extensively studied, mainly due to their diversified structural and magnetic properties [5-7]. Such double perovskites usually have full/complete rock-salt ordered structures because of the large difference in the oxidation states and sizes of the M^{2+} and W^{6+} cations [8]. Because magnetic M^{2+} cations are separated by non-magnetic W^{6+} cations, such perovskites can form a frustrated square lattice of spins [9]. Their magnetism arises from super-superexchange interactions, *M*−O−(W)−O−*M*, between disconnected MO_6 octahedra. Typically, the *M*/WO_6 octahedra undergo distortions and/or tilts in multiple directions to accommodate size mismatches caused by the substituted cations at the A and/or *M* sites.

A lot of different A_2MWO_6 double perovskites have been synthesized, and their structure types are sensitive to chemical substitutions (summarized in Ref. [10], **TABLEs SI and SII**, see also references [11-14] therein). The smaller ionic radius of Ca^{2+} (1.34 Å, compared to 1.44 Å for Sr^{2+} and 1.61 Å for Ba^{2+}, with the coordination number of 12 [15]) results in a considerable tilting of the alternating MO_6 (*M* = Mg, Ca, Mn, Fe, Co, and Ni) and WO_6 octahedra in a monoclinic structure with the space group $P2_1/n$ [16-20], although in the case of Ca_2ZnWO_6 the space group $Fm\bar{3}m$ was also reported [21]. The majority of the Sr_2MWO_6 compounds adopt a tetragonal $I4/m$ structure (*M* = Mg, Fe, Co, Ni, and Cu) [22-25], though when *M* = Ca, Mn, Zn, or Cd, the structure changes to the $P2_1/n$ symmetry, similar to the Ca-containing compounds [25-29]. For Ba_2MWO_6, the cubic $Fm\bar{3}m$ space group is observed for *M* = Mg, Mn, Fe, Co, Ni, Zn, and Cd [17,22,30-34], while Ba_2CaWO_6 and Ba_2CuWO_6 adopt an $I4/m$ structure [5,35]. Furthermore, it was reported that the symmetry of Sr_2FeWO_6 and Ba_2FeWO_6 can depend on different synthesis procedures [6].

Structural phase transitions in the A_2MWO_6 double perovskites have been extensively studied, particularly in the A = Sr compounds (see **TABLEs SI and SII** [10]). These

compounds typically undergo phase transitions from low-symmetry space groups to high-symmetry space groups with increasing temperature, involving partial or complete transformations among the monoclinic, tetragonal, and cubic crystal systems. For example, in the cuprate double perovskite Sr_2CuWO_6, the Cu−O−W bond angles within the (001) planes are nonlinear indicating the octahedral tilting, and the presence of the Jahn–Teller (JT) active ions Cu^{2+} leads to significant distortions of the CuO_6 octahedra [36]. With increasing temperature, the Cu−O−W bond angle of Sr_2CuWO_6 changes to 180° (at around 870 K), and the CuO_6 octahedra are elongated along the fourfold axis. The room-temperature *I*4/*m* structure undergoes a transition to a higher-symmetry structure, *I*4/*mmm*. At approximately 1190 K, the long-range cooperative JT distortion disappears, leading to a first-order transition from *I*4/*mmm* to *Fm*−3*m* [25,37].

Sr_2CuWO_6 and Ba_2CuWO_6 have also been intensively investigated for their interesting magnetic properties [5,9,38-40]. It was found that these two double perovskites exhibit low-dimensional antiferromagnetic (AFM) behavior which was associated with the cooperative JT effect of Cu^{2+} and the super-superexchange interaction between Cu^{2+} cations via an array of W^{6+} cations. The JT effect results in the orbital ordering and alignment of the short Cu-O_{ab} bonds in the (001) planes and long Cu-O_c bonds along the *c*-axis. The half-filling of the $3d_{x^2-y^2}$ orbitals facilitates strong magnetic interactions within the (001) planes, whereas magnetic interactions along the *c*-axis are much weaker. In alternating CuO_6 and WO_6 octahedra, the AFM ordering comes from the 180° Cu–O–W–O–Cu super-superexchange interactions within the (001) planes and interplanar interactions along the *c*-axis [38,40]. In addition, Sr_2CuWO_6 has recently been investigated as a catalytic material [41,42]. The solid solutions of Sr_2CuWO_6 and isostructural Sr_2CuTeO_6 develop a complex magnetically disordered quantum state [43,44] driven by quenched randomness [45,46].

Although all other members of Ca_2MWO_6 with *M* = Mg, Ca, Mn, Fe, Co, Ni, and Zn, Sr_2MWO_6 and Ba_2MWO_6 with *M* = Mg, Ca, Mn, Fe, Co, Ni, Cu, and Zn have been successfully synthesized, Ca_2CuWO_6 remains a missing compound in the A_2MWO_6 family. In this work, the Ca_2CuWO_6 double perovskite was successfully synthesized by a high-pressure, high-temperature method. It has a highly distorted structure, which is different from other members of the family. It crystallizes in a triclinic space group *P*−1

between 100 K and 1000 K and shows the onset of partial decomposition above 750 K. It demonstrates low-dimensional magnetic properties with a broad maximum of the magnetic susceptibility around 60 K caused by the dominant second-neighbor interactions within the deformed square planes of the Cu^{2+} ions. A long-range antiferromagnetic order takes place at T_N = 32 K. The solid solutions $Ca_{2-x}Sr_xCuWO_6$ with x = 0.5, 1, and 1.5 were also prepared. The x = 0.5 and 1 samples crystallize in the space group $P\bar{1}$ at room temperature, similar to the x = 0 sample, whereas the x = 1.5 sample crystallizes in the space group $P2_1/n$. The $Ca_{2-x}Sr_xCuWO_6$ samples also show low-dimensional magnetic behavior, T_N = 32–34 K, and magnetic field-induced transitions.

2. Experimental

Ca_2CuWO_6 and $Ca_{2-x}Sr_xCuWO_6$ were prepared under high-pressure and high-temperature conditions using a belt-type high-pressure machine. Ca_2CuWO_6 was prepared from a stoichiometric mixture of Ca_3WO_6, CuO, and WO_3 at 6 GPa and about 1370 K and 1570 K for 2 h in Au capsules. We also prepared Ca_2CuWO_6 at 6 GPa and about 2020 K for 0.5 h in Pt capsules. $Ca_{2-x}Sr_xCuWO_6$ with x = 0.5, 1, 1.5, and 2 were prepared from stoichiometric mixtures of Ca_3WO_6, Sr_2WO_5, CuO, and WO_3 at 6 GPa and about 1370 K for 2 h in Au capsules. After annealing at the target temperature, the samples were cooled down to room temperature (RT) by turning off the heating current, and the pressure was slowly released. All the samples had brownish yellow color (**TABLE SIII** [10]**)**. Ca_3WO_6 was prepared from a stoichiometric mixture of $CaCO_3$ and WO_3 by annealing in air at 1270 K for 96 h with several intermediate grindings. Sr_2WO_5 was prepared by the same method as Ca_3WO_6 but from a stoichiometric mixture of $SrCO_3$ and WO_3.

Laboratory X-ray powder diffraction (XRPD) data were collected at RT on a RIGAKU MiniFlex600 diffractometer using CuKα radiation (in a 2θ range of 5–100° with a step of 0.02°, and scan speed of 3°/min). Synchrotron XRPD data for Ca_2CuWO_6 were collected on the beamline BL02B2 of SPring-8 from 100 K to 900 K on heating in one run and from 600 K to 1000 K on heating in another run (using a fresh sample) [47]. The data were taken between 4.002° and 71.25° at 0.006° intervals in 2θ using a wavelength of λ = 0.61974 Å. The data with good statistics for structural refinements were collected

at 100 K and 295 K (for 400 s); the measurement time was 10 s at all other temperatures. Synchrotron XRPD data of the $Ca_{2-x}Sr_xCuWO_6$ samples (x = 0.5, 1.0, and 1.5) were measured at RT with the measurement time of 100 s. The samples were filled into open Lindemann glass (or quartz, for measurements up to 1000 K) capillary tubes (inner diameter: 0.2 mm), which were rotated during the measurements. The Rietveld analysis of all XRPD data was performed using the *RIETAN-2000* program [48].

Magnetic measurements were performed on a SQUID magnetometer (Quantum Design, MPMS3) between 2 and 300 K in an applied field of 100 Oe and 10 kOe under both zero-field-cooled (ZFC) and field-cooled on cooling (FCC) conditions. Isothermal magnetization measurements were performed at different temperatures between −70 and 70 kOe. No corrections were applied to raw magnetic data. Samples weights were also not corrected (to account for non-magnetic impurities). Specific heat was measured on a Quantum Design PPMS-9T instrument on cooling at magnetic fields of 0 Oe and 90 kOe.

Dielectric properties of Ca_2CuWO_6 were measured on a NOVOCONTROL Alpha-A High Performance Frequency Analyzer on cooling in the temperature range between 3.5 K and 300 K and the frequency range between 301 Hz and 665 kHz at zero magnetic field.

Differential scanning calorimetry (DSC) curves of the Ca_2CuWO_6 powder sample (33.29 mg) were recorded on a Mettler Toledo DSC1 STAR^e system between 300 K and 870 K in an open Al capsule with the heating/cooling rate of 10 K/min under N_2 flow. Two DSC runs were performed to check the reproducibility. DSC measurements were also performed for the Ca_2CuWO_6 powder sample (17.47 mg) between 300 K and 970 K in an open Pt capsule with the heating/cooling rate of 10 K/min under N_2 flow. Laboratory XRPD data were collected after the DSC experiments to check phase compositions after heating.

Magnetic exchange couplings were evaluated by density-functional-theory (DFT) band-structure calculations performed in the FPLO code [49] using the Perdew-Burke-Ernzerhof (PBE) flavor of the exchange-correlation potential [50] and the experimental crystal structure of Ca_2CuWO_6. Correlation effects in the Cu 3*d* shell were taken into account on the mean-field DFT+U level with the on-site Coulomb repulsion potential U_d = 8.5 eV, Hund's coupling J_d = 1 eV, and double-counting correction in the atomic limit

[51,52]. Exchange couplings were obtained from the superexchange model and, concurrently, from total energies of magnetically ordered states using the mapping procedure [53,54]. Magnetic susceptibility of the square-lattice antiferromagnet was obtained from quantum Monte-Carlo (QMC) simulations using the *loop* algorithm [55] of the ALPS package [56].

3. Results and discussion

3.1. Crystal structure and high-temperature behavior

Ca_2CuWO_6 perovskite could be prepared at 6 GPa at different temperatures between 1370 and 2020 K. However, the amounts of the $CaWO_4$ impurity were different (**FIG. S1 and TABLE SIV** [10]**)**. For a detailed characterization, we selected a sample prepared at 1570 K with the minimum amount of the $CaWO_4$ impurity. The RT crystal structure of Ca_2CuWO_6 was determined from the synchrotron XRPD data. The Rietveld refinement (**FIG. 1**) confirmed that Ca_2CuWO_6 crystallizes in the triclinic space group $P\bar{1}$ which has never been observed in the other members of the A_2MWO_6 family. **TABLE I** lists the structure parameters and suggests that all sites in the double perovskite structure are fully occupied. The low symmetry of the structure gives rise to four independent sites for the B cations, specifically designated as Cu1(1*e*), Cu2(1*b*), W1(1*d*), and W2 (1*g*). The crystal structure at 100 K was also refined, and the structural parameters are presented in **TABLE SV** (the Rietveld refinement fits are shown on **FIG. S2**) [10].

As shown in **FIG. 2a**, the low-symmetry crystal structure consists of alternating corner-shared CuO_6 and WO_6 octahedra in three crystallographic directions. The Ca atoms (Ca1 and Ca2) occupy the interstitial spaces between the octahedra. The two nonequivalent octahedra for both Cu and W sites gave two different arrangements of the CuO_6 ($Cu1O_6$ and $Cu2O_6$) and WO_6 ($W1O_6$ and $W2O_6$) octahedra resulting in the two different types of alternating layers along the *b* axis. One layer consists of the $Cu2O_6$ and $W1O_6$ octahedra (**FIG. 2b**), and another layer consists of the $Cu1O_6$ and $W2O_6$ octahedra (**FIG. 2c**). The bond lengths, bond angles, octahedral distortion parameter (Δ), and bond valence sums (BVS) [57] for Ca_2CuWO_6 at RT are summarized in **TABLE II**. The BVS values for both the Ca sites and Cu sites were close to the excepted values of +2, while the values for the W1 and W2 sites were slightly higher than +6. The Cu1-O6 bonds in the $Cu1O_6$ octahedra and the Cu2-O5 bonds in the $Cu2O_6$ octahedra (~2.4 Å) are

198 significantly longer than the other Cu-O bonds (~2.0 Å) showing that the CuO_6 octahedra
199 are elongated along the (−101) direction. On the other hand, the WO_6 octahedra are
200 slightly compressed along (−101). The highly distorted CuO_6 octahedra with the sizable
201 octahedral distortion parameter ($\Delta(CuO_6)$) can be ascribed to the JT effect of the Cu^{2+}
202 ions. The Cu–O–W angles between the CuO_6 and WO_6 octahedra in Ca_2CuWO_6 are
203 smaller than those of Sr_2CuWO_6 and Ba_2CuWO_6 [5] as expected because the ion size of
204 Ca^{2+} is smaller than Sr^{2+} and Ba^{2+} (1.34 Å for Ca^{2+}, 1.44 Å for Sr^{2+}, and 1.61 Å for Ba^{2+},
205 with a coordination number of 12) [15]. Therefore, the combination of the largest tilts
206 (among A_2CuWO_6) and strong JT effects could result in a strong structural distortion and
207 triclinic symmetry.
208 We note that the crystal structure of Ca_2CuWO_6 was predicted from the first-principles
209 calculations in the framework of the Materials Project, where two models were given in
210 space group *Cm* [58] and $P2_1/c$ [59]. However, the experimental structure does not match
211 with these two predictions (**FIGs. S3** [10]).
212 **FIG. 3** depicts the temperature dependence of the unit-cell parameters and volume
213 based on the in situ synchrotron XRPD measurements. The *a* lattice parameter first
214 decreases slightly from 100 to 225 K, then gradually increases from 225 to 450 K, and
215 starts to decline when the temperature exceeds 450 K. However, both *b* and *c* lattice
216 parameters monotonically increase on heating from 100 to 900 K. Therefore, Ca_2CuWO_6
217 demonstrates anisotropic thermal expansion above 450 K. The values of α and γ exhibit
218 a monotonically decreasing trend with increasing temperature, while the value of β
219 initially shows a slight increase before also following a consistent downward trend (**FIG.**
220 **3c**). Concurrently, the unit-cell volume (*V*) demonstrates a monotonically increasing trend
221 without any anomalies (**FIG. 3d**) with the volumetric coefficient of thermal expansion of
222 $3.61(14)\times10^{-5}$ K^{-1} between 500 K and 850 K. As illustrated in **FIGs. S4a-S4c** [10], the
223 diffraction peak positions shift slightly towards lower angles across the entire temperature
224 range due to heating, which can be attributed to thermal expansion effects. The refined
225 weight fraction of the $CaWO_4$ impurity started increasing above 750 K along with the
226 broadening of the corresponding reflections, and very broad new diffraction peaks
227 appeared, which can be assigned to Ca_3WO_6 impurity. Above 850 K, diffraction peaks
228 from the CuO impurity could be detected as well. Therefore, the Ca_2CuWO_6 double

perovskite partially decomposes above about 750 K. Despite this partial decomposition, all lattice parameters continue to change monotonically up to 900 K. Compared to the as-synthesized, original sample, the diffraction patterns (measured at RT) of the samples obtained after in-situ synchrotron XRPD heating experiments to 900 K and 1000 K exhibit significant changes (**FIG. S5** [10]). The $CaWO_4$ impurity content in the sample heated to 900 K increased from 3.3 wt% to 8.6 wt% (**FIG. S6a** [10]), and small amounts of Ca_3WO_6 and CuO could be detected. While in the sample heated to 1000 K, the $CaWO_4$ content rose to 24.9 wt%, the sample also contained 40.5 wt% Ca_3WO_6, and broad peaks from Cu_2O could be identified (**FIG. S6b** [10]). No noticeable anomalies were observed in the DSC curves. Therefore, the DSC measurements and high-temperature in situ synchrotron XRPD studies suggest that Ca_2CuWO_6 double perovskite (partly) decomposes above 750 K and does not undergo any structural phase transitions between 100 K and 750 K, thus preserving its triclinic symmetry in a broad temperature range.

3.2. Magnetic susceptibility

The temperature dependence of the magnetic susceptibilities for Ca_2CuWO_6 measured under applied magnetic fields of 10 kOe and 100 Oe is illustrated in **FIG. 4 and FIG. S7** [10], respectively. As shown in **FIG. 4**, a broad maximum of the magnetic susceptibility is observed at around 60 K originating from low-dimensional magnetism – a characteristic feature commonly observed in the A_2CuWO_6 double perovskites. The temperature at which these maxima occur serves as an indicator of the magnitude of the predominant AFM exchange interactions. With decreasing temperature, a long-range AFM order takes place below T_N (Néel temperature) = 32 K, as evidenced by peaks in the ZFC and FCC $d\chi/dT$ versus T curves (inset of **FIG. 4 and FIG. S7** [10]). The T_N value for Ca_2CuWO_6 was slightly higher than the T_N values of 28 K and 24 K reported for Ba_2CuWO_6 [60] and Sr_2CuWO_6 [39], respectively.

The inverse magnetic susceptibilities exhibit the behavior consistent with the Curie–Weiss law at elevated temperatures above approximately 200 K. The FCC data, measured under an applied magnetic field of 10 kOe, were accurately fitted to the following Curie–Weiss equation within the temperature range of 200 K to 295 K:

$$\chi(T) = \mu_{\text{eff}}^2 \, N(3k_{\text{B}}(T-\theta))^{-1}$$

Here μ_{eff} is the effective magnetic moment, N is Avogadro's number, k_B is Boltzmann's constant, and θ is the Curie–Weiss temperature. The observed experimentally determined effective magnetic moment, μ_{eff} = 1.776(3) μ_B, aligns closely with the spin-only theoretical value, $\mu_{\text{cal}} = g\sqrt{S(S+1)} \approx 1.732\ \mu_B$, calculated for the Cu^{2+} ions, where S = ½ and g = 2. This agreement confirms that Cu^{2+} is the sole contributor to the magnetic properties of Ca_2CuWO_6. The μ_{eff} value is comparable to those of Ba_2CuWO_6 [61] and Sr_2CuWO_6 [5,40]. The negative Weiss temperature (θ = –88.6(12) K) confirms the dominant AFM interactions (**TABLE III**).

The isothermal magnetization curve (M versus H) for Ca_2CuWO_6 at T = 5 K is illustrated in **FIG. S8** [10]. There was almost no hysteresis near the origin (zero magnetic field) suggesting a purely AFM state. Furthermore, as shown in **FIG. 5 and Table SVI** [10], the M versus H curves at different temperatures indicate a magnetic field-induced transition at 28 kOe (at 2 K and 5 K), 29 kOe (at 10 K), 30 kOe (at 15 K), 32 kOe (at 20 K), and 36 kOe (at 25 K).

While the low-symmetry crystal structure of Ca_2CuWO_6 allows for multiple nonequivalent superexchange pathways, our DFT calculations (**Sec. 3.5**) show that the dominant interactions connect second-neighbor Cu^{2+} ions, which build deformed square lattices associated with the Cu1 and Cu2 sites, respectively (**Table IV**). These interpenetrating square lattices are connected by the weaker nearest-neighbor couplings (**FIG. 8**) that lead to a moderate frustration akin to the J_1-J_2 square lattice model [62]. The experimental magnetic susceptibility of Ca_2CuWO_6 can be then described using the high-temperature series expansion (HTSE) for the J_1-J_2 square lattice model [63]. The respective fit extends down to 80 K and returns J_1 = 18 K, J_2 = 65 K (g = 2.10, χ_0 = -5.3×10^{-5} emu/mol), see **FIG. 4**. Alternatively, one could neglect the weaker nearest-neighbor couplings and use QMC simulations for the nonfrustrated square-lattice model with J = 63 K (g = 1.90, χ_0 = 8.5×10^{-5} emu/mol) that satisfactorily describes the data down to T_N, albeit showing a slightly different curvature at 100–200 K (**FIG. 4**). The resulting J value should be seen as an effective coupling within the deformed square lattices of Cu1 and Cu2.

3.3. Heat capacity

Specific heat data plotted as C_p/T versus T are shown in **FIG. 6**. A very weak and sharp anomaly was observed at $T_N = 32$ K at $H = 0$ Oe confirming the transition toward a long-range AFM ordered state. The fact that this transition is almost unaffected by the magnetic field of 90 kOe (inset of **FIG. 6**) gives additional evidence that Ca_2CuWO_6 is a robust antiferromagnet. In magnetic insulators, the specific heat capacity is primarily governed by lattice contributions at higher temperatures and magnetic contributions at lower temperatures. The lattice contribution was estimated using the experimental specific heat of the Ca_2CaWO_6 double perovskite without magnetic cations (between 2 and 46 K) and the experimental specific heat of the Ca_2MnWO_6 double perovskite (between 48 and 80 K) as described in Ref. [64]. We calculated the magnetic entropy, S_m, by integrating the difference between C_p and the lattice contribution. The expected magnetic entropy for spin-½ is $S_m = R\ln 2 \approx 5.76$ J K^{-1} mol^{-1}, where $R = 8.314$ J K^{-1} mol^{-1} is the universal gas constant. The calculated S_m of Ca_2CuWO_6 at $T = 80$ K is 2.8 J K^{-1} mol^{-1}, about half of the expected value. The reduced value of S_m in Ca_2CuWO_6 could be caused by the overestimation of the lattice contribution. However, the precise estimation of the lattice contribution is difficult as Ca_2CuWO_6 crystallizes in a different space group and in a highly distorted structure in comparison with other members of the family. Moreover, with the dominant exchange coupling of 63 K, a partial release of the magnetic entropy also above 80 K can be expected. The magnetic entropy below T_N was about 1.2 J K^{-1} mol^{-1}. In other words, more than half of the entropy (estimated in a way described above) is released above T_N, thus corroborating the low-dimensional nature of the Ca_2CuWO_6 magnetism.

3.4. Dielectric properties

FIG. 7 shows the temperature dependence of the dielectric constant, which was nearly frequency-independent between 3.5 and 100 K. No anomalies, kinks, or peaks were observed in the dielectric constant at $T_N = 32$ K. The high dielectric constant in the low-frequency region at higher temperatures was primarily caused by a Maxwell-Wagner contribution. Therefore, no magnetodielectric effects were detected in the Ca_2CuWO_6 double perovskite in comparison with the $(Ca_{2-x}Mn_x)MnWO_6$ and Ca_2MnWO_6 double perovskites [64].

3.5. Magnetic model

Triclinic symmetry of Ca_2CuWO_6 with two nonequivalent Cu sites renders the magnetic model of this material more complex compared to Sr_2CuWO_6. Therefore, we used DFT calculations to assess individual exchange couplings via two complementary methods, superexchange theory and mapping analysis. **FIG. 8** shows the metallic band structure of Ca_2CuWO_6, which is calculated on the PBE level and does not include correlations that are responsible for opening the band gap. This band structure can be used for identifying relevant electronic states of the material. The Fermi level is crossed by two bands with the predominant Cu $d_{x^2-y^2}$ character that corresponds to the highest-energy crystal-field level of Cu^{2+} in the distorted octahedral coordination. Each of the two bands is formed by Cu1 and Cu2, respectively, with only a weak hybridization. This separation of the orbital characters indicates that the magnetic sublattices of Cu1 and Cu2 are largely decoupled. Indeed, the hopping parameters extracted from the Wannier fit [65] of the two $d_{x^2-y^2}$ bands reveal stronger couplings within each sublattice and much weaker couplings between the sublattices (**Table IV**). Each sublattice represents a deformed square lattice (rectangular lattice) lying in the (10-1) plane of the crystal structure. Whereas the Cu1 sublattice is almost regular, the Cu2 sublattice shows a sizable difference between the couplings along the [010] and [101] directions within the plane. The leading interplane hopping is about 5 meV, at least one order of magnitude smaller than the in-plane hoppings. Therefore, Ca_2CuWO_6 should be understood as a quasi-2D antiferromagnet, in agreement with the experiment.

Our mapping analysis confirms these results. The Cu1 and Cu2 sites form interpenetrating rectangular lattices with the dominant interactions J_{21a}, J_{21b}, J_{22a}, and J_{22b}. These rectangular lattices are connected by the weaker frustrated couplings J_{1a} and J_{1b} (**Table IV**). Overall, the magnetic model of Ca_2CuWO_6 can be interpreted as a distorted version of the J_1-J_2 frustrated square lattice. Previous studies showed that such deformations almost do not influence the magnetic susceptibility above T_N [66]. Therefore, the fitted values of J_1 and J_2 should be seen as the averaged nearest-neighbor and second-neighbor couplings, respectively: $J_1 = (J_{1a}+J_{1b})/2$ and $J_2 = (J_{21a}+J_{21b}+J_{22a}+J_{22b})/4$. From the DFT results (**Table IV**), one finds $J_1 = 9$ K and $J_2 = 59$ K in a good agreement with the fitted values of 18 K and 65 K, respectively.

Despite its triclinic distortion, Ca_2CuWO_6 features the same mechanism of the exchange couplings as the other Cu^{2+} double perovskites. The second-neighbor couplings are amplified by the low-lying *d*-states of W^{6+}, similar to Sr_2CuWO_6 and at odds with Sr_2CuTeO_6 where the *p*-states of Te^{6+} facilitate nearest-neighbor couplings (J_1) and suppress second-neighbor couplings (J_2) [9,67].

3.6. Sr^{2+} doping

Solid solutions $Ca_{2-x}Sr_xCuWO_6$ with x = 0.5, 1, and 1.5 were also prepared to study the doping effects in Ca_2CuWO_6 and its evolution toward the extensively studied Sr_2CuWO_6 [5,25,36,38-40,68-71]. XRPD data for the $Ca_{2-x}Sr_xCuWO_6$ samples with x = 0.5, 1, and 1.5 are illustrated in **FIG. S9** [10] and compared with Ca_2CuWO_6 (x = 0) and Sr_2CuWO_6 (x = 2), prepared under similar synthesis conditions. With the increase in the Sr^{2+} concentration (x), the main impurity changes from $CaWO_4$ (for x = 0, 0.5, and 1) to the high-pressure modification of $Sr_3W_2O_9$ [72] (for x = 1.5 and 2). Our analysis showed that the x = 0.5 and 1 samples retained the space group $P\bar{1}$. However, the application of this triclinic model to the x = 1.5 sample resulted in the following refined angles, α = 89.997(2)° and γ = 89.998(2)°, suggesting that the symmetry is higher. Therefore, the structure of the x = 1.5 sample was refined in the space group $P2_1/n$, which is a direct supergroup of $P\bar{1}$ with the same cell dimensions. (**FIGs. S10-S12 and TABLEs SVII - SX** [10]). We also note that only a few extremely weak reflections with $h + k + l = 2n + 1$ were observed experimentally in the x = 1.5 sample. In other words, the structure of the x = 1.5 sample can also be well refined in the $I2/m$ model (**FIG. S12 and TABLEs SVIII and SX** [10]). We further emphasize that the $P2_1/n$ symmetry is usually assigned for monoclinic members of the A_2MWO_6 family, but the $P2_1/n$ model has a monoclinic angle β between the $\sqrt{2}a_p$ and $2a_p$ lattice parameters (where a_p is the parameter of the cubic perovskite subcell). On the other hand, the $P2_1/n$ model of the x = 1.5 sample has its monoclinic angle β between the $\sqrt{2}a_p$ and $\sqrt{2}a_p$ lattice parameters. No DSC anomalies were found in the x = 1.5 sample between 300 K and 870 K suggesting the absence of structural phase transitions. The compositional dependence of the cell parameters and volume obtained from the synchrotron XRPD data is presented in **FIG. S13** [10]**.** The *b* and *c* parameters increased linearly, whereas the *a* parameter decreased gradually with

increasing x. Additionally, the α and γ parameters decreased linearly with increasing x, whereas the β parameter remained almost constant. The volume V increased linearly as expected following the incorporation of the larger Sr^{2+} ions. The effect of Sr^{2+} doping on the lattice parameters of $Ca_{2-x}Sr_xCuWO_6$ was similar to the effect of temperature on the lattice parameters of Ca_2CuWO_6.

The magnetic susceptibility and isothermal magnetization curves for the $Ca_{2-x}Sr_xCuWO_6$ samples with x = 0.5, 1, and 1.5 are given on **FIGs. S14-S16** [10], and their Curie–Weiss fit parameters are summarized in **TABLE III**. They also showed the quasi-2D magnetic behavior and magnetic field-induced transitions (**FIGs. S17-S22** [10]). The T_N remained nearly the same in the $Ca_{2-x}Sr_xCuWO_6$ samples with x = 0.5 (T_N = 32 K), 1 (T_N = 33 K), and 1.5 (T_N = 34 K) (**FIGs. S23-S24** [10]). This observation is somewhat unexpected, considering that the T_N of Sr_2CuWO_6 (x = 2) was reported to be 24 K [39]. Therefore, the symmetry lowering in the $Ca_{2-x}Sr_xCuWO_6$ samples with $0 \le x \le 1.5$ enhances T_N. The magnetic field corresponding to the field-induced transition at different temperatures also increases noticeably. For example, at 25 K, the corresponding magnetic field is 36 kOe for x = 0, and it increased to 42 kOe for x = 0.5 and 49 kOe for x = 1.

In simple ABO_3 perovskites with direct B–O–B exchange interactions, magnetic phase transition temperatures are highly sensitive to the value of B–O–B angles and, therefore, to the A-cation size. Magnetic phase transition temperatures usually decrease with decreasing the size of the A cations [73]. However, in the A_2MWO_6 double perovskites with the M−O−(W)−O−M super-superexchange interactions, the opposite tendency is observed wherein the more distorted samples with A = Ca have higher magnetic phase transition temperatures (**TABLE SI** [10]). Our results for Ca_2CuWO_6 are in agreement with this tendency.

4. Conclusions

In conclusion, Ca_2CuWO_6 double perovskite – a missing member in the family of the A_2MWO_6 double perovskites – was successfully prepared by a high-pressure, high-temperature method. Ca_2CuWO_6 has a highly distorted structure and different symmetry in comparison with other members of the family. It crystallizes in a triclinic space group

$P\bar{1}$ between 100 K and 1000 K; however, it shows partial decomposition above 750 K upon heating in air. Magnetic susceptibility data and density-functional calculations consistently show a quasi-2D antiferromagnetic behavior, with the deformed square lattice of the Cu^{2+} ions dominated by the second-neighbor exchange couplings of about 60 K. A long-range antiferromagnetic order takes place at T_N = 32 K, and a magnetic field-induced transition was observed below T_N. The solid solutions $Ca_{2-x}Sr_xCuWO_6$ with x = 0.5 and 1 also crystallize in the space group $P\bar{1}$ at room temperature, while the x = 1.5 sample has a $P2_1/n$ structure. $Ca_{2-x}Sr_xCuWO_6$ samples show similar quasi-2D magnetic behavior, T_N = 32–34 K, and magnetic field-induced transitions.

Acknowledgements

This work was partially supported by a Grant-in-Aid for Scientific Research (No. JP22H04601) from the Japan Society for the Promotion of Science. Synchrotron radiation was used at the powder diffraction beamline BL02B2 at SPring-8 with the permission from the Japan Synchrotron Radiation Research Institute (Proposal Numbers: 2023B1676 and 2024B1825). We thank Dr. S. Kobayashi and Dr. Mori Yuki for their help at BL02B2 of SPring-8. MANA was supported by the World Premier International Research Center Initiative (WPI), MEXT, Japan.

REFERENCES

[1] S. Vasala and M. Karppinen, $A_2B'B''O_6$ perovskites: A review, Prog. Solid State Chem. **43**, 1 (2015).

[2] K. I. Kobayashi, T. Kimura, H. Sawada, K. Terakura, and Y. Tokura, Room-temperature magnetoresistance in an oxide material with an ordered double-perovskite structure, Nature **395**, 677 (1998).

[3] M. DeMarco, H. A. Blackstead, J. D. Dow, M. K. Wu, D. Y. Chen, F. Z. Chien, M. Haka, S. Toorongian, and J. Fridmann, Magnetic phase transition in superconducting $Sr_2YRu_{0.95}Cu_{0.05}O_6$ observed by the ^{99}Ru Mössbauer effect, Phys. Rev. B **62**, 14301 (2000).

[4] Z. Szotek, W. M. Temmerman, A. Svane, L. Petit, and H. Winter, Electronic structure of half-metallic double perovskites, Phys. Rev. B **68**, 104411 (2003).

[5] D. Iwanaga, Y. Inaguma, and M. Itoh, Crystal Structure and Magnetic Properties of B-Site Ordered Perovskite-type Oxides $A_2CuB'O_6$ (A=Ba, Sr; B'=W, Te), J. Solid State Chem. **147**, 291 (1999).

[6] A. K. Azad, S. G. Eriksson, A. Mellergård, S. A. Ivanov, J. Eriksen, and H. Rundlöf, A study on the nuclear and magnetic structure of the double perovskites A_2FeWO_6 (A = Sr, Ba) by neutron powder diffraction and reverse Monte Carlo modeling, Mater. Res. Bull. **37**, 1797 (2002).

[7] A. Muñoz, J. A. Alonso, M. T. Casais, M. J. Martínez-Lope, and M. T. Fernández-Díaz, Crystal and magnetic structure of the complex oxides Sr_2MnMoO_6, Sr_2MnWO_6 and Ca_2MnWO_6: a neutron diffraction study, J. Phys.: Condens. Matter **14**, 8817 (2002).

[8] A. M. Abakumov, A. A. Tsirlin, and E. V. Antipov, in *Comprehensive Inorganic Chemistry II: From Elements to Applications*, edited by J. Reedijk, and K. R. Poeppelmeier (Elsevier, Amsterdam, 2013), pp. 1.

[9] O. Mustonen, S. Vasala, H. Mutch, C. I. Thomas, G. B. G. Stenning, E. Baggio-Saitovitch, E. J. Cussen, and M. Karppinen, Magnetic interactions in the S = 1/2 square-lattice antiferromagnets Ba_2CuTeO_6 and Ba_2CuWO_6: parent phases of a possible spin liquid, Chem. Commun. **55**, 1132 (2019).

[10] See Supplemental Material for information on A_2MWO_6 compounds, structure parameters of $Ca_{2-x}Sr_xCuWO_6$ with x = 0 (100 K), 0.5, 1, and 1.5, details of XRD, color, and magnetic measurements. The Supplemental Material also contains Refs. [11-14].

[11] M. Retuerto, J. A. Alonso, M. J. Martínez-Lope, M. García-Hernández, C. A. López, M. d. C. Viola, J. C. Pedregosa, and M. T. Fernández-Díaz, A Structural and Magnetic Study of the Series of Double Perovskites $Ca_2Fe_{1+x}W_{1-x}O6$, Eur. J. Inorg. Chem. **2009**, 3750 (2009).

[12] Z. FU and W. LI, Phase transition, phase transition mechanism and crystal structure of a new compound-Ca_2FeWO_6, Sci. China, Ser. A **38**, 974 (1995).

[13] A. K. Eriksson, S. G. Eriksson, S. A. Ivanov, C. S. Knee, and H. Rundlöf, Phase Transitions of the Magnetoelectric A_2NiMoO_6 (A = Ba, Sr) and Ca_2NiWO_6 by Neutron Diffraction, Ferroelectrics **339**, 235 (2006).

[14] C. Su, X.-T. Zeng, K. Sun, D. Sheptyakov, Z. Chen, X.-L. Sheng, H. Li, and W. Jin, Type-II antiferromagnetic ordering in the double perovskite oxide Sr_2NiWO_6, Phys. Rev. B **108**, 054416 (2023).

[15] R. Shannon, Revised effective ionic radii and systematic studies of interatomic distances in halides and chalcogenides, Acta Crystallogr. Sect. A **32**, 751 (1976).
[16] S. J. Patwe, S. N. Achary, M. D. Mathews, and A. K. Tyagi, Crystal structure and thermal expansion behavior of Ca_2MgWO_6, Mater. Chem. Phys. **98**, 486 (2006).
[17] B. E. Day, N. D. Bley, H. R. Jones, R. M. McCullough, H. W. Eng, S. H. Porter, P. M. Woodward, and P. W. Barnes, Structures of ordered tungsten- or molybdenum-containing quaternary perovskite oxides, J. Solid State Chem. **185**, 107 (2012).
[18] A. K. Azad, S. A. Ivanov, S. G. Eriksson, J. Eriksen, H. Rundlöf, R. Mathieu, and P. Svedlindh, Nuclear and magnetic structure of Ca_2MnWO_6: A neutron powder diffraction study, Mater. Res. Bull. **36**, 2485 (2001).
[19] R. Vidya, P. Ravindran, A. Kjekshus, and H. Fjellvåg, Huge magneto-optical effects in half-metallic double perovskites, Phys. Rev. B **70**, 184414 (2004).
[20] M. J. Martínez-Lope, J. A. Alonso, M. T. Casais, and M. T. Fernández-Díazb, Preparation, Crystal and Magnetic Structure of the Double Perovskites Ca_2TWO_6 (T = Co, Ni), Z. Naturforsch. B **58**, 127 (2003).
[21] K. V. Dabre and S. J. Dhoble, Synthesis and photoluminescence properties of Eu^{3+}, Sm^{3+} and Pr^{3+} doped Ca_2ZnWO_6 phosphors for phosphor converted LED, J. Lumin. **150**, 55 (2014).
[22] S. J. Patwe, S. N. Achary, M. D. Mathews, and A. K. Tyagi, Synthesis, phase transition and thermal expansion studies on M_2MgWO_6 (M = Ba^{2+} and Sr^{2+}) double perovskites, J. Alloy. Compd. **390**, 100 (2005).
[23] T. S. Chan, R. S. Liu, S. F. Hu, and J. G. Lin, Structure and physical properties of double perovskite compounds Sr_2FeMO_6 (M = Mo, W), Mater. Chem. Phys. **93**, 314 (2005).
[24] M. C. Viola, M. J. Martínez-Lope, J. A. Alonso, J. L. Martínez, J. M. De Paoli, S. Pagola, J. C. Pedregosa, M. T. Fernández-Díaz, and R. E. Carbonio, Structure and magnetic properties of Sr_2CoWO_6: An ordered double perovskite containing Co^{2+}(HS) with unquenched orbital magnetic moment, Chem. Mater. **15**, 1655 (2003).
[25] M. Gateshki, J. Igartua, and E. Hernandez-Bocanegra, X-ray powder diffraction results for the phase transitions in Sr_2MWO_6 (M = Ni, Zn, Co, Cu) double perovskite oxides, J. Phys.: Condens. Matter **15**, 6199 (2003).
[26] A. Faik, J. M. Igartua, G. J. Cuello, F. Jiménez-Villacorta, G. R. Castro, and L. Lezama, Crystal structures and temperature-induced phase transitions of $Sr_2Mn^{2+}W^{6+}O_6$, and of its transformation to $Sr_2Mn^{3+}W^{6+}O_{6+\delta}$, J. Mol. Struct. **933**, 53 (2009).
[27] M. Gateshki and J. M. Igartua, Crystal structures and phase transitions of the double-perovskite oxides Sr_2CaWO_6 and Sr_2MgWO_6, J. Phys.: Condens. Matter **16**, 6639 (2004).
[28] A. K. Azad, S. Ivanov, S. G. Eriksson, H. Rundlöf, J. Eriksen, R. Mathieu, and P. Svedlindh, Structural and magnetic properties of the double perovskite Sr_2MnWO_6, J. Magn. Magn. Mater. **237**, 124 (2001).
[29] M. Gateshki, J. M. Igartua, and A. Faik, Crystal structure and phase transitions of Sr_2CdWO_6, J. Solid State Chem. **180**, 2248 (2007).
[30] H. Mutch, O. Mustonen, H. C. Walker, P. J. Baker, G. B. G. Stenning, F. C. Coomer, and E. J. Cussen, Long- and short-range magnetism in the frustrated double perovskite Ba_2MnWO_6, Phys. Rev. Mater. **4**, 014408 (2020).

[31] M. M. Saad H.-E and N. Rammeh, Crystal structure, electronic and magnetic properties of double perovskite Ba_2FeWO_6: A combined experimental–theoretical study, Phys. B **481**, 217 (2016).
[32] C. A. López, M. E. Saleta, J. Curiale, and R. D. Sánchez, Crystal field effect on the effective magnetic moment in A_2CoWO_6 (A = Ca, Sr and Ba), Mater. Res. Bull. **47**, 1158 (2012).
[33] J. Bijelić, D. Tatar, M. Sahu, Z. Jagličić, and I. Djerdj, Size reduction-induced properties modifications of antiferromagnetic dielectric nanocrystalline Ba_2NiMO_6 (M = W, Te) double perovskites, Oxf. Open Mater. Sci. **1**, 1 (2021).
[34] D. E. Bugaris, J. P. Hodges, A. Huq, and H.-C. zur Loye, Crystal growth, structures, and optical properties of the cubic double perovskites Ba_2MgWO_6 and Ba_2ZnWO_6, J. Solid State Chem. **184**, 2293 (2011).
[35] K. Yamamura, M. Wakeshima, and Y. Hinatsu, Structural phase transition and magnetic properties of double perovskites $Ba_2Ca\mathit{M}O_6$ (M = W, Re, Os), J. Solid State Chem. **179**, 605 (2006).
[36] M. W. Lufaso, W. R. Gemmill, S. J. Mugavero, Y. Lee, T. Vogt, and H.-C. z. Loye, Compression mechanisms of symmetric and Jahn–Teller distorted octahedra in double perovskites: A_2CuWO_6 (A = Sr, Ba), Sr_2CoMoO_6, and La_2LiRuO_6, J. Solid State Chem. **179**, 3556 (2006).
[37] P. E. Tomaszewski, Structural phase transitions in crystals. I. Database, Phase Transit. **38**, 127 (1992).
[38] S. Vasala, M. Avdeev, S. Danilkin, O. Chmaissem, and M. Karppinen, Magnetic structure of Sr_2CuWO_6, J. Phys.: Condens. Matter **26**, 496001 (2014).
[39] S. Vasala, H. Saadaoui, E. Morenzoni, O. Chmaissem, T.-S. Chan, J.-M. Chen, Y.-Y. Hsu, H. Yamauchi, and M. Karppinen, Characterization of magnetic properties of Sr_2CuWO_6 and Sr_2CuMoO_6, Phys. Rev. B **89**, 134419 (2014).
[40] S. Vasala, J. G. Cheng, H. Yamauchi, J. B. Goodenough, and M. Karppinen, Synthesis and characterization of $Sr_2Cu(W_{1-x}Mo_x)O_6$: A quasi-two-dimensional magnetic system, Chem. Mater. **24**, 2764 (2012).
[41] J. Zhu, Y. Zhang, Z. Chen, Z. Zhang, X. Tian, M. Huang, X. Bai, X. Wang, Y. Zhu, and H. Jiang, Superexchange-stabilized long-distance Cu sites in rock-salt-ordered double perovskite oxides for CO_2 electromethanation, Nat. Commun. **15**, 1565 (2024).
[42] E. Hua, S. Jin, S. Ni, and X. Xu, Double perovskite compounds A_2CuWO_6(A = Sr and Ba) with p-type semiconductivity for photocatalytic water oxidation under visible light illumination, Inorg. Chem. Front. **6**, 2096 (2019).
[43] O. Mustonen, S. Vasala, E. Sadrollahi, K. P. Schmidt, C. Baines, H. C. Walker, I. Terasaki, F. J. Litterst, E. Baggio-Saitovitch, and M. Karppinen, Spin-liquid-like state in a spin-1/2 square-lattice antiferromagnet perovskite induced by d^{10}-d^0 cation mixing, Nat. Commun. **9**, 1085 (2018).
[44] X. Hu, D. M. Pajerowski, D. Zhang, A. A. Podlesnyak, Y. Qiu, Q. Huang, H. Zhou, I. Klich, A. I. Kolesnikov, M. B. Stone *et al.*, Freezing of a Disorder Induced Spin Liquid with Strong Quantum Fluctuations, Phys. Rev. Lett. **127**, 017201 (2021).
[45] E. Fogh, O. Mustonen, P. Babkevich, V. M. Katukuri, H. C. Walker, L. Mangin-Thro, M. Karppinen, S. Ward, B. Normand, and H. M. Rønnow, Randomness and

frustration in a $S = 1/2$ square-lattice Heisenberg antiferrom, Phys. Rev. B **105**, 184410 (2022).
[46] O. H. J. Mustonen, E. Fogh, J. A. M. Paddison, L. Mangin-Thro, T. Hansen, H. Y. Playford, M. Diaz-Lopez, P. Babkevich, S. Vasala, M. Karppinen *et al.*, Structure, Spin Correlations, and Magnetism of the $S = 1/2$ Square-Lattice Antiferromagnet $Sr_2CuTe_{1-x}W_xO_6$ ($0 \leqslant x \leqslant 1$), Chem. Mater. **36**, 501 (2024).
[47] S. Kawaguchi, M. Takemoto, K. Osaka, E. Nishibori, C. Moriyoshi, Y. Kubota, Y. Kuroiwa, and K. Sugimoto, High-throughput powder diffraction measurement system consisting of multiple MYTHEN detectors at beamline BL02B2 of SPring-8, Rev. Sci. Instrum. **88**, 085111 (2017).
[48] F. Izumi and T. Ikeda, A Rietveld-Analysis Programm RIETAN-98 and its Applications to Zeolites, Mater. Sci. Forum **321–324**, 198 (2000).
[49] K. Koepernik and H. Eschrig, Full-potential nonorthogonal local-orbital minimum-basis band-structure scheme, Phys. Rev. B **59**, 1743 (1999).
[50] J. P. Perdew, K. Burke, and M. Ernzerhof, Generalized Gradient Approximation Made Simple, Phys. Rev. Lett. **77**, 3865 (1996).
[51] V. V. Mazurenko, M. V. Valentyuk, R. Stern, and A. A. Tsirlin, Nonfrustrated interlayer order and its relevance to the Bose-Einstein condensation of magnons in $BaCuSi_2O_6$, Phys. Rev. Lett. **112**, 107202 (2014).
[52] P. Bag, N. Ahmed, V. Singh, M. Sahoo, A. A. Tsirlin, and R. Nath, Low-dimensional magnetism of $BaCuTe_2O_6$, Phys. Rev. B **103**, 134410 (2021).
[53] H. J. Xiang, E. J. Kan, S.-H. Wei, M. H. Whangbo, and X. G. Gong, Predicting the spin-lattice order of frustrated systems from first principles, Phys. Rev. B **84**, 224429 (2011).
[54] A. A. Tsirlin, Spin-chain magnetism and uniform Dzyaloshinsky-Moriya anisotropy in BaV_3O_8, Phys. Rev. B **89**, 014405 (2014).
[55] S. Todo and K. Kato, Cluster Algorithms for General- S Quantum Spin Systems, Phys. Rev. Lett. **87**, 047203 (2001).
[56] A. F. Albuquerque, F. Alet, P. Corboz, P. Dayal, A. Feiguin, S. Fuchs, L. Gamper, E. Gull, S. Gürtler, A. Honecker *et al.*, The ALPS project release 1.3: Open-source software for strongly correlated systems, J. Magn. Magn. Mater. **310**, 1187 (2007).
[57] N. E. Brese and M. O'Keeffe, Bond-Valence Parameters for Solids, Acta Crystallogr. Sect. B **47**, 192 (1991).
[58] K. Persson, Materials Data on Ca_2CuWO_6 (SG:8) by Materials Project, DOI: 10.17188/1321528 (2014).
[59] K. Persson, Materials Data on Ca_2CuWO_6 (SG:14) by Materials Project, DOI: 10.17188/1321209 (2014).
[60] Y. Todate, W. Higemoto, K. Nishiyama, and K. Hirota, Magnetic ordering in ordered complex Cu perovskite probed by μSR and neutron diffraction, J. Phys. Chem. Solids **68**, 2107 (2007).
[61] Y. Todate, Antiferromagnetism and Frustration in Ba_2CuWO_6, J. Phys. Soc. Jpn. **70**, 337 (2001).
[62] P. Chandra and B. Doucot, Possible spin-liquid state at large S for the frustrated square Heisenberg lattice, Phys. Rev. B **38**, 9335 (1988).
[63] H. Rosner, R. R. P. Singh, W. H. Zheng, J. Oitmaa, and W. E. Pickett, High-temperature expansions for the $J_1 - J_2$ Heisenberg models: Applications to ab initio calculated models for Li_2VOSiO_4 and Li_2VOGeO_4, Phys. Rev. B **67**, 014416 (2003).

[64] A. A. Belik, Hybrid multiferroic behavior in the double perovskite $(Ca_{0.5}Mn_{1.5})MnWO_6$, Chem. Mater. **36**, 7604 (2024).
[65] K. Koepernik, O. Janson, Y. Sun, and J. van den Brink, Symmetry-conserving maximally projected Wannier functions, Phys. Rev. B **107**, 235135 (2023).
[66] A. A. Tsirlin and H. Rosner, Extension of the spin-1/2 frustrated square lattice model: The case of layered vanadium phosphates, Phys. Rev. B **79**, 214417 (2009).
[67] V. M. Katukuri, P. Babkevich, O. Mustonen, H. C. Walker, B. Fåk, S. Vasala, M. Karppinen, H. M. Rønnow, and O. V. Yazyev, Exchange Interactions Mediated by Nonmagnetic Cations in Double Perovskites, Phys. Rev. Lett. **124**, 077202 (2020).
[68] M. Gateshki and J. M. Igartua, Second-order structural phase transition in Sr_2CuWO_6 double-perovskite oxide, J. Phys.: Condens. Matter **15**, 6749 (2003).
[69] J. C. Grivel and P. Norby, Subsolidus phase relations of the $SrO–WO_3–CuO$ system at 800 °C in air, J. Alloy. Compd. **513**, 304 (2012).
[70] H. C. Walker, O. Mustonen, S. Vasala, D. J. Voneshen, M. D. Le, D. T. Adroja, and M. Karppinen, Spin wave excitations in the tetragonal double perovskite Sr_2CuWO_6, Phys. Rev. B **94**, 06441 (2016).
[71] O. Mustonen, S. Vasala, K. P. Schmidt, E. Sadrollahi, H. C. Walker, I. Terasaki, F. J. Litterst, E. Baggio-Saitovitch, and M. Karppinen, Tuning the $S = 1/2$ square-lattice antiferromagnet $Sr_2Cu(Te_{1-x}W_x)O_6$ from Néel order to quantum disorder to columnar order, Phys. Rev. B **98**, 064411 (2018).
[72] D. Urushihara, T. Asaka, K. Fukuda, and H. Sakurai, High-pressure synthesis and crystal structure of the strontium tungstate $Sr_3W_2O_9$, Acta Crystallogr. Sect. C **74**, 120 (2018).
[73] E. Bousquet and A. Cano, Non-collinear magnetism in multiferroic perovskites, J. Phys.: Condens. Matter **28**, 123001 (2016).

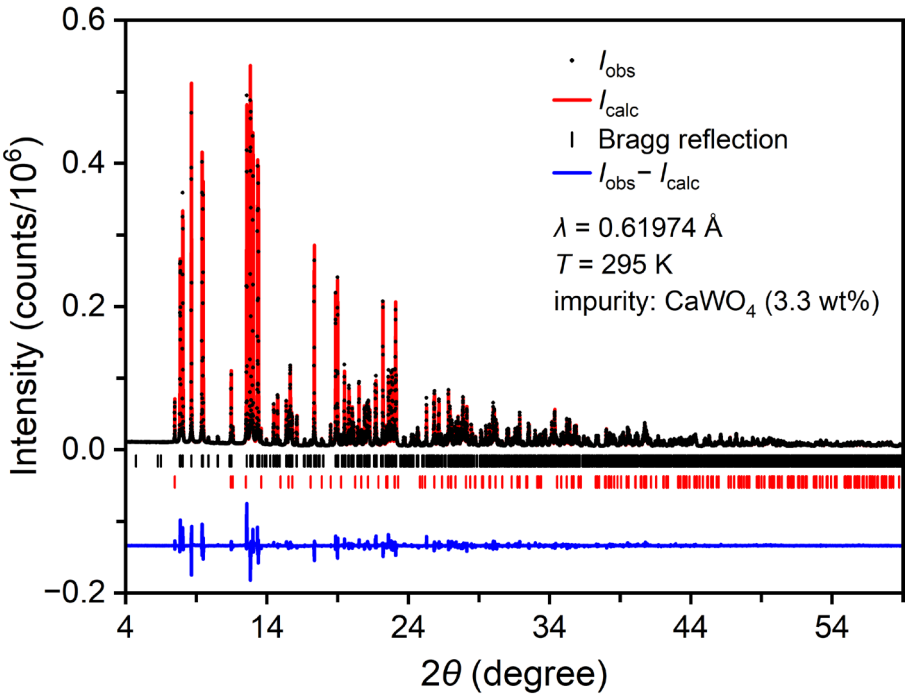

646 **FIG. 1.** Fragments of the experimental (black circles), calculated (red line), and
647 difference (blue line at the bottom) synchrotron X-ray powder diffraction (XRPD)
648 patterns of Ca_2CuWO_6 at $T = 295$ K. The tick marks show possible Bragg reflection
649 positions of the main perovskite phase (the first black row) and $CaWO_4$ impurity (the
650 second red row).

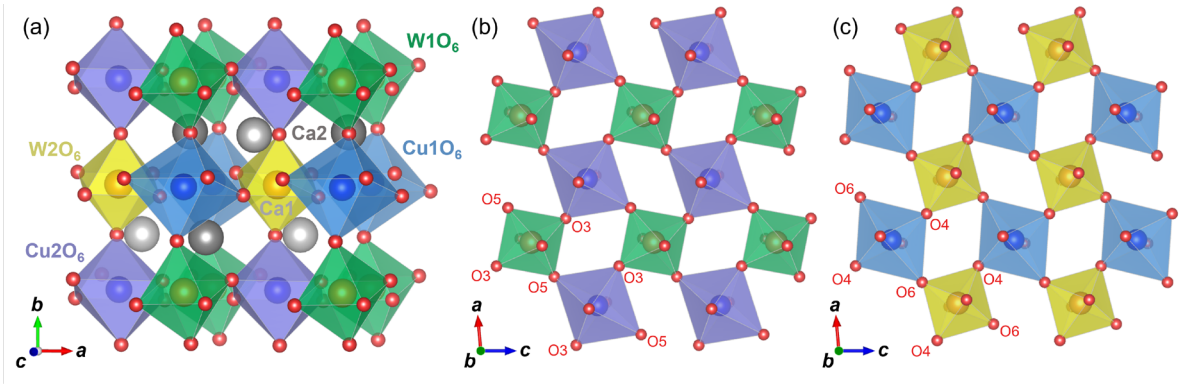

651 **FIG. 2**. (a) Fragments of the Ca_2CuWO_6 crystal structure with the *P*–1 space group in a
652 polyhedral presentation. The $Cu1O_6$, $Cu2O_6$, $W1O_6$, and $W2O_6$ octahedra are shown.
653 The Ca atoms are presented by large grey spheres. Two types of octahedral
654 arrangements along the *b* axis with (b) $Cu2O_6$-$W1O_6$ and (c) $Cu1O_6$-$W2O_6$ types.

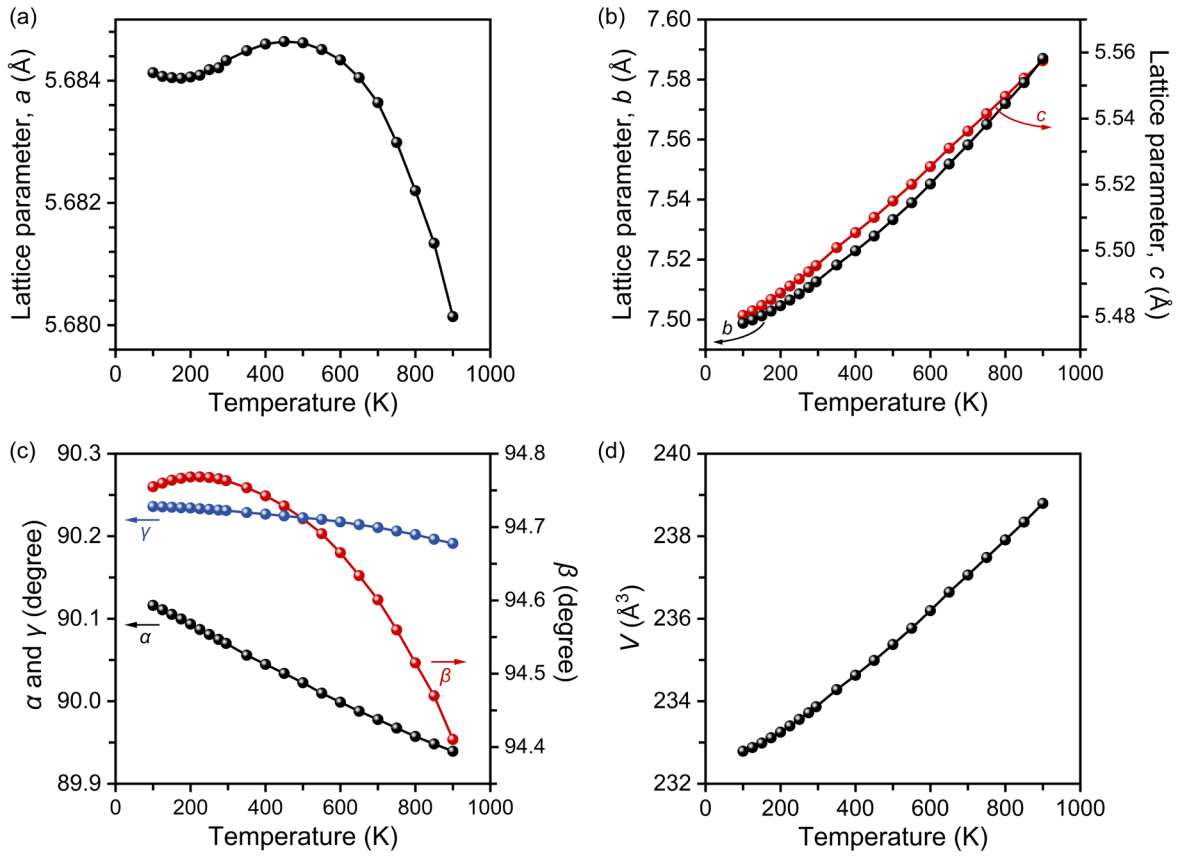

655 **FIG. 3.** Unit-cell parameters (a, b, c, α, β, and γ) and volume (V) as a function of
656 temperature for Ca_2CuWO_6 from synchrotron XRPD data measured on heating.

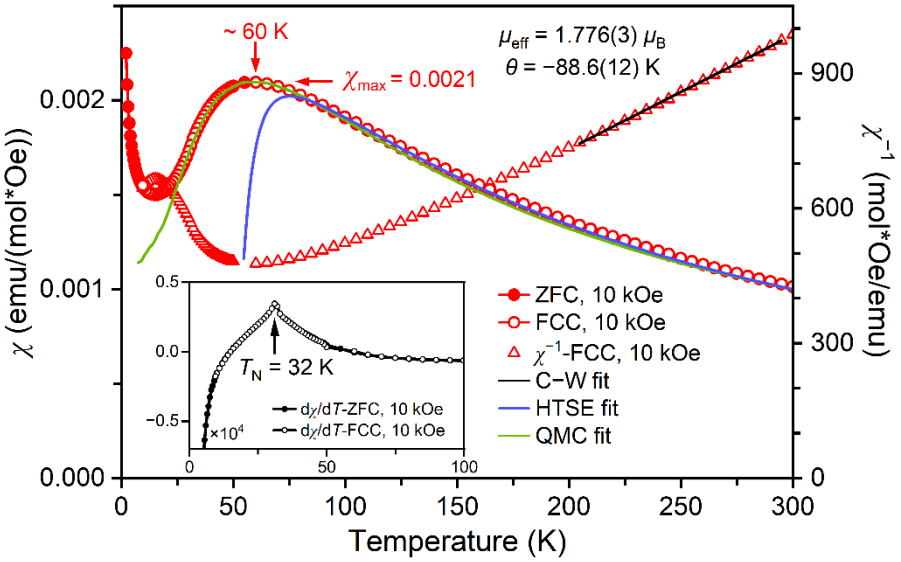

FIG. 4. ZFC (filled red circles) and FCC (empty red circles) dc magnetic susceptibility ($\chi = M/H$) curves for Ca_2CuWO_6 measured at 10 kOe. The black line shows the Curie–Weiss fit (C–W fit) of the FCC χ^{-1} versus T curve. The HTSE and QMC fits, as described in the text, are also shown. The inset presents the dχ/dT versus T curves.

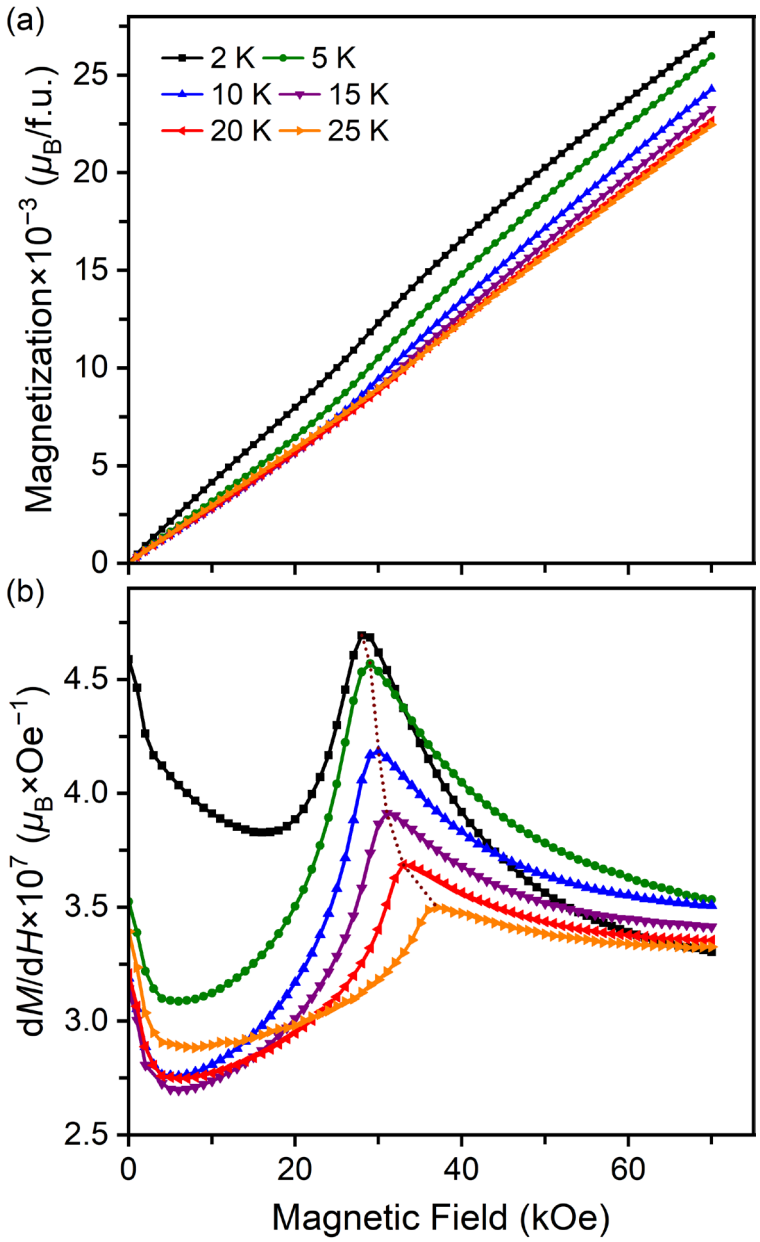

662 **FIG. 5.** (a) *M* versus *H* curves and (b) derivative of magnetization curves (d*M*/d*H*
663 versus *H*) for Ca_2CuWO_6 at different temperatures. The dotted line is drawn for eye.

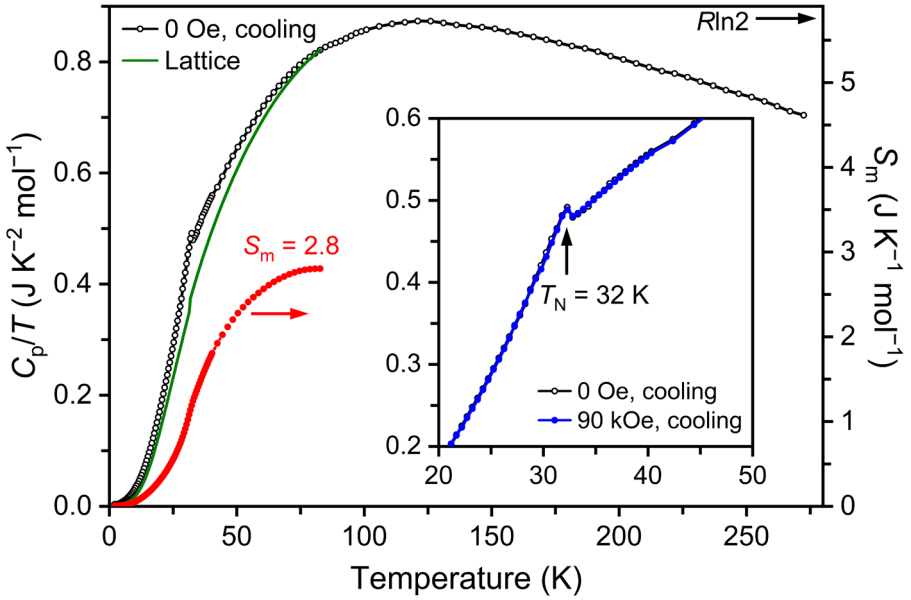

664 **FIG. 6.** Specific heat data, C_p/T (empty circles; measured on cooling at $H = 0$ Oe) and
665 magnetic entropy, S_m (filled red circles), of Ca_2CuWO_6 as a function of T are shown in
666 the left and right y axes, respectively. The green line shows the estimated lattice
667 contribution (see the text). The inset presents the C_p/T versus T measured on cooling at
668 $H = 0$ Oe (empty circles) and 90 kOe (filled blue circles) in the vicinity of T_N.

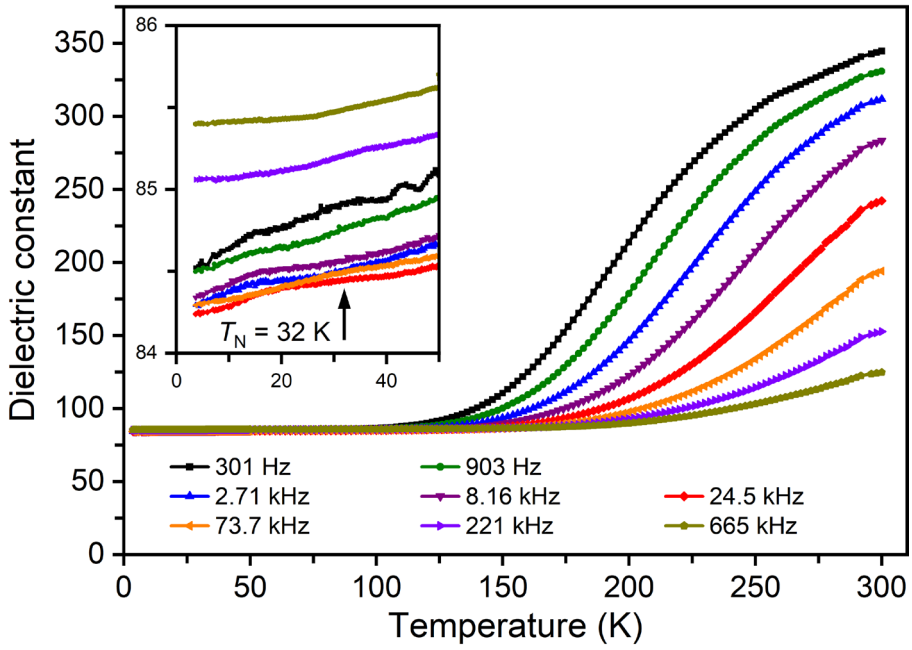

669 **FIG. 7.** Frequency-dependent (from 301 Hz to 665 kHz) dielectric constant of
670 Ca_2CuWO_6 as a function of temperature measured at $H = 0$ Oe on heating. The inset
671 shows a zoomed part in the vicinity of T_N.

672

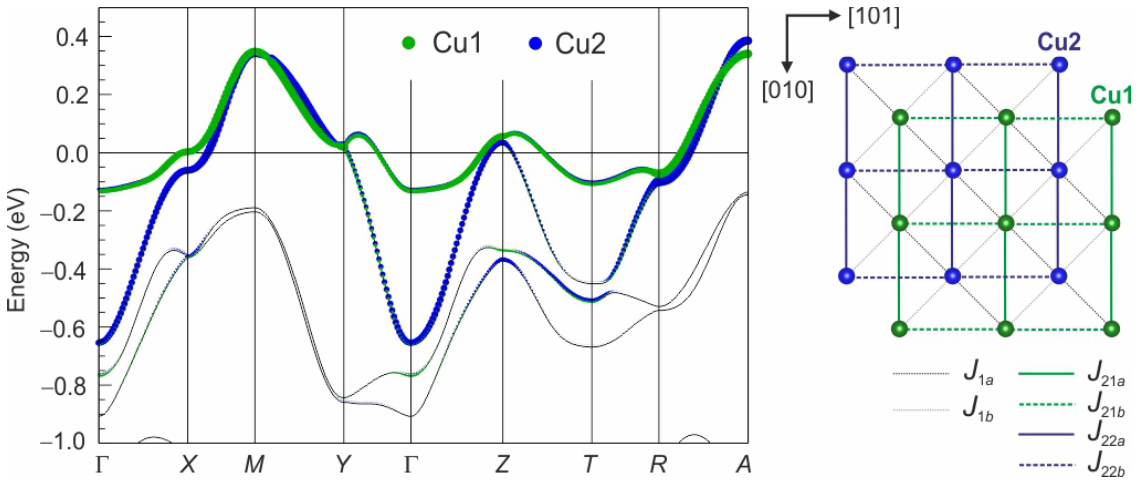

673

674 **FIG. 8.** Left: PBE band structure of Ca_2CuWO_6 with the band weights due to the Cu1
675 and Cu2 $d_{x^2-y^2}$ orbitals. The Fermi level is at zero energy. Right: spin lattice of
676 Ca_2CuWO_6 (see Table IV for the list of the exchange couplings).

677 **TABLE I.** Structure parameters of Ca_2CuWO_6 at 295 K from synchrotron X-ray powder
678 diffraction data.

site	WP	*g*	*x*	*y*	*z*	B_{iso} (Å^2)
Ca1	2*i*	1	0.0547(5)	0.2522(3)	1.0021(5)	0.71(5)
Ca2	2*i*	1	0.5519(5)	0.2497(3)	0.5150(5)	0.77(5)
Cu1	1*e*	1	0.5	0.5	0	1.12(8)
Cu2	1*b*	1	0	0	0.5	0.11(6)
W1	1*d*	1	0.5	0	0	0.44(2)
W2	1*g*	1	0	0.5	0.5	0.23(2)
O1	2*i*	1	0.4720(12)	0.2454(11)	0.0867(13)	0.25(14)
O2	2*i*	1	0.9736(13)	0.2590(11)	0.4270(14)	0.59(15)
O3	2*i*	1	0.3119(11)	0.0467(9)	0.7016(13)	0.59(14)
O4	2*i*	1	0.7059(12)	0.5521(10)	0.3037(13)	0.92(15)
O5	2*i*	1	0.2283(12)	0.9438(9)	0.1658(13)	0.96(15)
O6	2*i*	1	0.8353(12)	0.4563(10)	0.7766(12)	0.73(13)

679 Synchrotron powder X-ray diffraction (λ = 0.61974 Å); *d* range used in the refinement:
680 from 0.532 Å to 8.879 Å. Crystal system: triclinic; space group: *P*−1 (No. 2, origin choice
681 1), *Z* = 2. Molecular weight: 423.5384 g/mol. *a* = 5.68435(1) Å, *b* = 7.51261(2) Å, *c* =
682 5.49548(1) Å, α = 90.0703(2)°, β = 94.7634(2)°, γ = 90.2310(2)°, and *V* = 233.8677(8)
683 Å^3; R_{wp} = 5.94%, R_p = 4.50%, R_I = 2.26%, and R_F = 1.19%. WP = Wyckoff position. *g* is
684 the occupation factor.

685 **TABLE II.** Selected bond lengths (Å), angles (deg), octahedral distortion parameters
686 (Δ), and bond valence sums (BVS) for Ca_2CuWO_6 at T = 295 K.

Ca1–O1	2.379(8)	Ca2–O1	2.360(8)
Ca1–O2	2.418(9)	Ca2–O2	2.485(8)
Ca1–O3	2.768(8)	Ca2–O3	2.670(8)
Ca1–O4	2.696(8)	Ca2–O3	2.336(8)
Ca1–O5	2.651(8)	Ca2–O4	2.719(8)
Ca1–O5	2.311(8)	Ca2–O4	2.362(8)
Ca1–O6	2.554(8)	Ca2–O5	2.531(8)
Ca1–O6	2.282(8)	Ca2–O6	2.581(8)
BVS (Ca1)	2.06	BVS (Ca2)	1.99
Cu1–O1 ×2	1.980(8)	Cu2–O2 ×2	1.991(8)
Cu1–O4 ×2	2.008(7)	Cu2–O3 ×2	2.040(7)
Cu1–O6 ×2	2.375(7)	Cu2–O5 ×2	2.374(7)
BVS (Cu1)	2.01	BVS (Cu2)	1.92
Δ ($Cu1O_6$)	7.2×10^{-3}	Δ ($Cu2O_6$)	6.4×10^{-3}
W1–O5 ×2	1.903(7)	W2–O2 ×2	1.857(8)
W1–O1 ×2	1.914(8)	W2–O6 ×2	1.879(7)
W1–O3 ×2	1.915(7)	W2–O4 ×2	1.946(7)
BVS (W1)	6.17	BVS (W2)	6.49
Δ ($W1O_6$)	8.1×10^{-6}	Δ ($W2O_6$)	4.0×10^{-4}
Cu1–O1–W1	149.3(5)	Cu2–O2–W2	155.0(5)
Cu1–O4–W2	146.5(5)	Cu2–O3–W1	146.3(4)
Cu1–O6–W2	150.3(4)	Cu2–O5–W1	148.1(4)

687 $\mathrm{BVS} = \sum_{i=1}^{N} v_i$, $v_i = \exp[(R_0 - l_i)/B]$, N is the coordination number, l_i is a bond length, B
688 = 0.37, $R_0(Ca^{2+})$ = 1.967, $R_0(Cu^{2+})$ = 1.679, $R_0(W^{6+})$ = 1.921. $\Delta = (1/N)\sum_{i=1}^{N}[(l_i -$
689 $l_{\mathrm{av}})/l_{\mathrm{av}}]^2$, where $l_{\mathrm{av}} = (1/N)\sum_{i=1}^{N} l_i$ is the average distance.

TABLE III. Lattice parameters of $Ca_{2-x}Sr_xCuWO_6$ (x = 0, 0.5, 1, 1.5, and 2) at T = 295 K from the synchrotron[a] and laboratory[b] X-ray powder diffraction data, the Néel temperatures (T_N), and main parameters extracted from the magnetic susceptibility curves: position (T_{max}) and height (χ_{max}) of the susceptibility maximum, the effective moment and Curie-Weiss temperature (from the Curie–Weiss fits), as well as J_1 and J_2 (from the HTSE fits above 80 K for x = 0, above 90 K for x = 0.5, 1, 1.5, and above 100 K for x = 2; up to 400 K for all samples).

x	0[a]	0.5[a]	1[a]	1.5[a]	2[b]
space group	$P\bar{1}$	$P\bar{1}$	$P\bar{1}$	$P2_1/n$	$I4/m$
a (Å)	5.68435(1)	5.68310(3)	5.67677(3)	5.67514(2)	5.4284(1)
b (Å)	7.51261(2)	7.56989(3)	7.62931(4)	7.68165(3)	= a
c (Å)	5.49548(1)	5.56063(3)	5.62368(3)	5.65900(3)	8.4155(2)
α (°)	90.0703(2)	89.9575(6)	89.8954(5)	90	90
β (°)	94.7634(2)	94.8187(4)	94.7683(3)	94.8384(3)	90
γ (°)	90.2310(2)	90.2037(4)	90.1552(5)	90	90
V (Å^3)	233.8677(8)	238.374(2)	242.717(2)	245.822(2)	247.986(9)
μ_{eff} (μ_B/f.u.)	1.776(3)	1.693(4)	1.689(3)	1.907(9)	1.649(9)
θ (K)	–88.6(12)	–83.6(9)	–101.2(11)	–163(4)	–155(4)
T_N (K)	32	32	33	34	24 [34]
χ_{max} (emu/(mol*Oe))	0.0021	0.0020	0.0017	0.0017	0.0013
T_{max} (K)	60	55	65	72	72
$T_{max}/\|\theta\|$	0.677	0.658	0.642	0.442	0.465
J_1 (K)	18	15	9	6	6
J_2 (K)	65	68	78	85	97

TABLE IV. Magnetic couplings in Ca_2CuWO_6: interatomic distances d_i, hopping parameters t_i (from the Wannier fits), and exchange couplings J_i (from the mapping analysis).

		d_i (Å)	t_i (meV)	J_i (K)
J_{1a}	Cu1–Cu2	5.323	43	9
J_{1b}	Cu1–Cu2	5.343	43	9
J_{21a}	Cu1–Cu1	7.513	78	54
J_{21b}	Cu1–Cu1	7.571	80	51
J_{22a}	Cu2–Cu2	7.513	95	80
J_{22b}	Cu2–Cu2	7.571	79	50